applied sciences

Article

Non-Contact Monitoring of Operating Conditions for Solar Cells in a Photovoltaic Module Using a Surface Potential Meter for Detecting the Risk of Fire

Ryo Shimizu, Yasuyuki Ota, Akira Nagaoka, Kenji Araki * and Kensuke Nishioka

Faculty of Engineering, University of Miyazaki, Miyazaki 889-2192, Japan;
hk15022@student.miyazaki-u.ac.jp (R.S.); y-ota@cc.miyazaki-u.ac.jp (Y.O.);
nagaoka.akira.m0@cc.miyazaki-u.ac.jp (A.N.); nishioka@cc.miyazaki-u.ac.jp (K.N.)
* Correspondence: araki.kenji.j4@cc.miyazaki-u.ac.jp; Tel.: +81-985-58-7366

Featured Application: Solar panel fire accident diagnosis, analysis, and prediction.

Abstract: Fires in photovoltaic modules are caused by hot spots, which are typically monitored by thermal images. This method helps visualize the hot spot, but it is affected by the environment (solar irradiance, wind, ambient temperature) and is not reproducible. Assessing the heat dissipation of the hot cell can be used for alternative assessment of the fire risk. This method was validated by comparing the value measured by the surface potential meter and the module potential measured directly by adding a bypass measurement circuit. The substantial reverse-bias voltage caused by mismatching or partial shading (depending on the operating conditions) leads to local heat consumption of the partially shaded solar cells and potentially causes fire. The fire risk can be assessed in the worst-case conditions (ex. 1380 W/m^2 solar irradiance) by non-contact measurement of the reverse-bias voltage and calculating the heat dissipation and temperature rise. This work suggested that −13 V is the criterion and was close to the known value of reverse voltage for Si cells. The current technology inspects solar cells before assembly to the module, and there is no way of inspecting in the product test or detecting after degradation that can be covered by the proposed method in this work.

Keywords: photovoltaic module; hot spot; fire; surface potential meter; mismatching loss

Citation: Shimizu, R.; Ota, Y.; Nagaoka, A.; Araki, K.; Nishioka, K. Non-Contact Monitoring of Operating Conditions for Solar Cells in a Photovoltaic Module Using a Surface Potential Meter for Detecting the Risk of Fire. *Appl. Sci.* **2023**, *13*, 10391. https://doi.org/10.3390/app131810391

Academic Editors: Manuela Sechilariu, Saleh Cheikh-Mohamad and Berk Celik

Received: 12 July 2023
Revised: 14 September 2023
Accepted: 14 September 2023
Published: 17 September 2023

1. Introduction

After experiencing the first oil crisis in 1973 and other energy crises, Japan promoted the diversification of energy sources to create a society that does not rely heavily on fossil fuels. After the first oil crisis, dependence on fossil fuels decreased from 94% to 81.2% in 2010. However, owing to the shutdown of all nuclear power plants after the Great East Japan Earthquake in 2011, the operation of thermal power plants increased, and dependence on fossil fuels rose again to 87.4% in FY2017 (statistics by the government were made by fiscal year) [1]. Based on these events, the Japanese energy industry must solve three problems: the depletion of fossil fuels, global warming, and safe and stable energy supply.

Expectations regarding renewable energy solving this problem are increasing. Renewable energy refers to energy that can be used repeatedly by utilizing phenomena that occur naturally on Earth, such as sunlight, wind power, and geothermal heat, rather than the energy generated from fossil fuels, such as oil, coal, and natural gas. Specifically, renewable energy includes photovoltaic, solar thermal, wind, geothermal, and hydraulic power generation. The share of power generation from renewable energy increased, and photovoltaic power generation is increasing.

The rapid spread of solar power generation is due to the feed-in tariff (FIT) system for renewable energy introduced in 2012 and the following excellent features of solar power generation.

1. Inexhaustible energy source

A solar cell directly converts light energy from the sun into electrical energy via the photoelectric effect of a semiconductor. If we could convert 100% of the solar energy that hits the Earth, the amount of energy would be so large that it would cover the world's annual energy consumption in just one hour and never run out.

2. Maintenance, automation, and uncrewed operations are easy.

Unlike thermal power plants, there are no rotating machines or high-temperature, high-pressure parts; therefore, no mechanical wear occurs, and no lubricating oil is required. The operation and maintenance are simple, and the system can easily be automated or can be operated unmanned.

3. Installation locations are not limited.

Because it can be installed in unused spaces, such as roofs and walls, there is no need to prepare new land for installation.

4. Because of its modular structure, it is suitable for mass production and has a considerable scale advantage.

Because solar cells are manufactured with a compact module structure, they are highly mass-producible. Line manufacturing is complex because other equipment require large parts.

In recent years, owing to global warming caused by the depletion of fossil fuels and rising greenhouse gases, renewable energy sources, such as solar, hydroelectric, wind, and geothermal power, have attracted attention. Among these, photovoltaic power generation is desirable because it has fewer location restrictions than other methods [2–8]. Advances in solar cell technology require rapid and detailed performance measurement methods [9,10]. Solar cells can be used outdoors by covering multiple PV cells with fillers, glass, and backsheets. However, once a module has been processed, it cannot be disassembled. A typical method for measuring and evaluating solar cell performance involves examining the I–V characteristics of a PV module. However, after processing the module, it is only possible to measure and evaluate the performance of the PV module as a whole [11–15]. Detailed performance measurements and performance evaluations after processing are necessary to further improve the quality of the PV modules.

Infrared thermography, electroluminescence (EL) inspection, and photoluminescence (PL) inspection are visible performance measurement/evaluation methods other than I–V measurement techniques. Infrared thermography identifies defects such as hot spots inside PV modules by examining the heat dissipation distribution of PV modules. EL inspection applies an electric field to the PV module and captures near-infrared light when excited electrons return to the ground state. Using this infrared light, it is possible to check for claps in the cells of the PV module and disconnection/connection failure of the intercollector. Similar to the EL inspection, the PL inspection is based on imaging near-infrared light when excited electrons return to their ground state. However, PL inspection uses light irradiation, rather than an electric field, to excite electrons. These methods evaluate PV cell defects, such as the clap and forbidden band of PV cells [16]. However, quantitative infrared thermography analysis remains controversial. In addition, EL/PL inspection requires reliable equipment. Furthermore, these methods have been established as performance measurement and evaluation methods for manufacturing silicon wafers and PV cells. However, their application in PV modules remains limited.

The current and voltage of the PV cells and modules are essential indicators for evaluating their performance. In addition, if the current and voltage of the element cells in a PV module can be measured, a more detailed performance evaluation is possible.

Previous studies have investigated non-contact potential measurements of PV modules. This study investigated a method for identifying faulty modules in PV arrays based on non-contact potential measurements of the PV modules. Because the purpose of this study was failure diagnosis, we focused only on the potential of the PV module. However, when performing performance measurements and evaluations, it is preferable to measure the current and voltage, which directly reflect the performance.

In addition to performance, safety is also essential for PV systems. Several cases of fire caused by PV systems were reported and investigated [17–19]. A local temperature rise caused these fires, called hot spots, and their temperature rise was the concentration of the energy loss of the solar cells owing to current-mismatching loss [20–24]. Thermal images typically monitor and detect these local losses [25–33]. However, it is essential to detect early symptoms using non-contact and non-destructive test methods and to quantify the modeling and measurement of the degree of concentration of the mismatching loss, for example, xx W loss (xx may be obtained by measurement) in this particular solar cell. The fire risk is also known to organic photovoltaics [34].

In addition to these approaches, such diagnostic and monitoring functions can be implemented in the solar system using power optimizers. They detect it by the current balance and shut down the damaged or degraded strings. However, physical, non-destructive, and non-contact inspection approaches are demanded for detailed information about the risk.

A standard Inspection method for the fire risk assessment is temperature imaging by IR camera. This inspection evaluates the status (temperature) in a specific environment (solar irradiance, ambient temperature, and wind). The criteria may be if the hot-spot temperature is substantially high (more than the firing point). Although it visually shows the risk of the temperature rise, the inspected value varies by measurement environment and is not reproducible. The inspection method proposed in this work evaluates the potential (magnitude of heat source that raises temperature). The advantage of this method is to anticipate the worst-case temperature and judge if it is higher than the firing points. The differences between the new measurement method and the standard IR camera inspection are summarized in Table 1. The proposed method detects the reverse-bias voltage of each cell [35] and calculates the dissipated heat by multiplication of the circuit current. The conversion to the temperature from the dissipated heat of the solar cell can be calculated by multiplication of the proportional coefficient [36].

Table 1. Differences between the new measurement method and the standard IR camera inspection.

Item	IR Camera	This Method
Visual presentation	Yes	No
Indicator	Temperature	Heat
Sensing	IR radiation	Electric field
Scaling to the worst-case	Not applicable	Applicable
Measurement error	1 °C	1% of the fire risk threshold

The inspection based on the endurance to the reverse-bias voltage is introduced in the component test (each solar cell). The typical criterion is less than −13 V [37–39]. However, the current technology inspects solar cells before assembly to the module, and there is no way of examining them in the product test (module level) or detecting the risk after degradation. These can be covered by the proposed method in this work.

One of the advantages of this non-contact and non-destructive inspection approach is the test without disconnecting the electrical circuit. If the modules are accessible by technicians on the roofs of houses or a rack of solar power plants, all they need is to approach the probe on the surface of the module. Disconnecting modules from the string for inspection is unnecessary, and onsite checking with keeping the circuit is possible. For rough detection, measured bias voltage at the non-standard solar irradiation level can be scaled and corrected by the low linear proportion. However, regarding the reproducible discrimination of the fire risk, taking a reverse-bias voltage under a given circuit current or controlled solar irradiance will be necessary.

Therefore, in this study, we verified a high-accuracy voltage detection method for the PV module and the element cells in the PV module by non-contact potential measurement in two states: the open state and the short-circuited state. To improve the quality, we also discuss a method for detecting degraded cells in PV modules and quantifying the magnitude of the local heat potentially leading to fire using the method based on the *I*–*V* characteristics.

2. Materials and Methods

2.1. Photovoltaic Modules, in General

Figure 1 shows the structure of a superstrate-type solar cell module, which is a typical solar cell module. The smallest unit in a solar battery is the cell. A crystalline Si solar cell comprises 210 mm, 182 mm, or 166 mm wafers and is half or 1/3 cut. The voltage of one solar cell is as low as around 0.7 V. Therefore, dozens of solar cells are connected in series in a solar cell module. In addition, because the PV module is installed outdoors, it has a structure in which multiple cells are covered with white tempered glass, fillers, a back sheet, and an aluminum frame. The internal cells are connected using an interconnector, the ends of which are pulled out from the rear surface and connected to a terminal output cable inside the terminal box to remove the generated power.

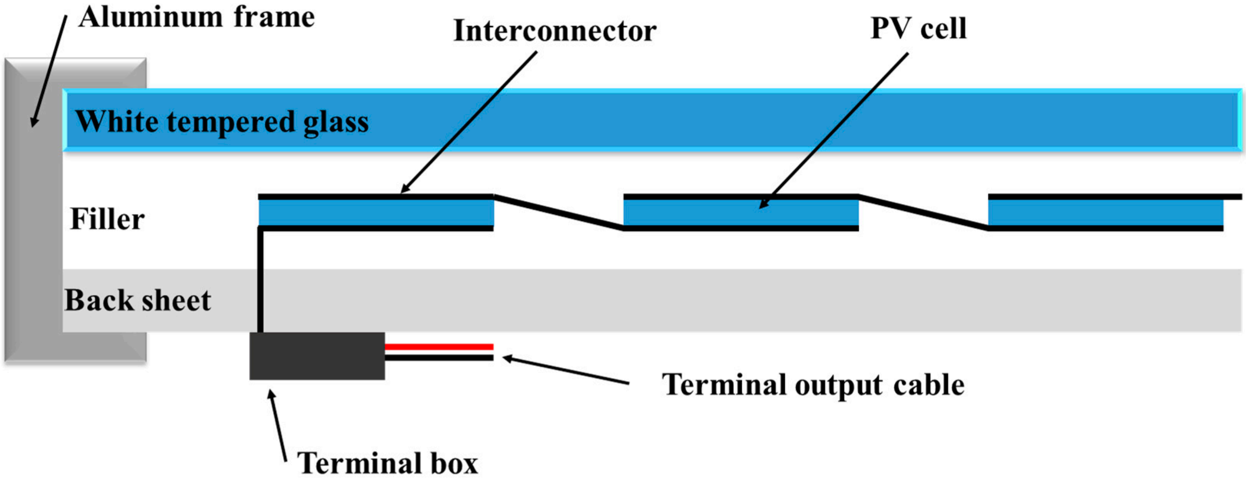

Figure 1. Typical structure of photovoltaic modules.

A bypass diode was installed inside the solar cell module. Figure 2 shows a schematic diagram of the operation of the solar-cell module. When the solar cell that constitutes a solar cell module does not generate power in the shade, the resistance of the cell increases, hindering the flow of current and generating heat owing to resistance loss. To prevent this, a bypass diode is connected in parallel to the solar-cell module as a current path that bypasses the shaded portion. Bypass diodes are typically placed in each string of the solar modules, corresponding to 20 or fewer solar cells. Bypass diodes can reduce the impact (decrease in current) on the remaining strings when some cells stop generating power owing to shadows or failures.

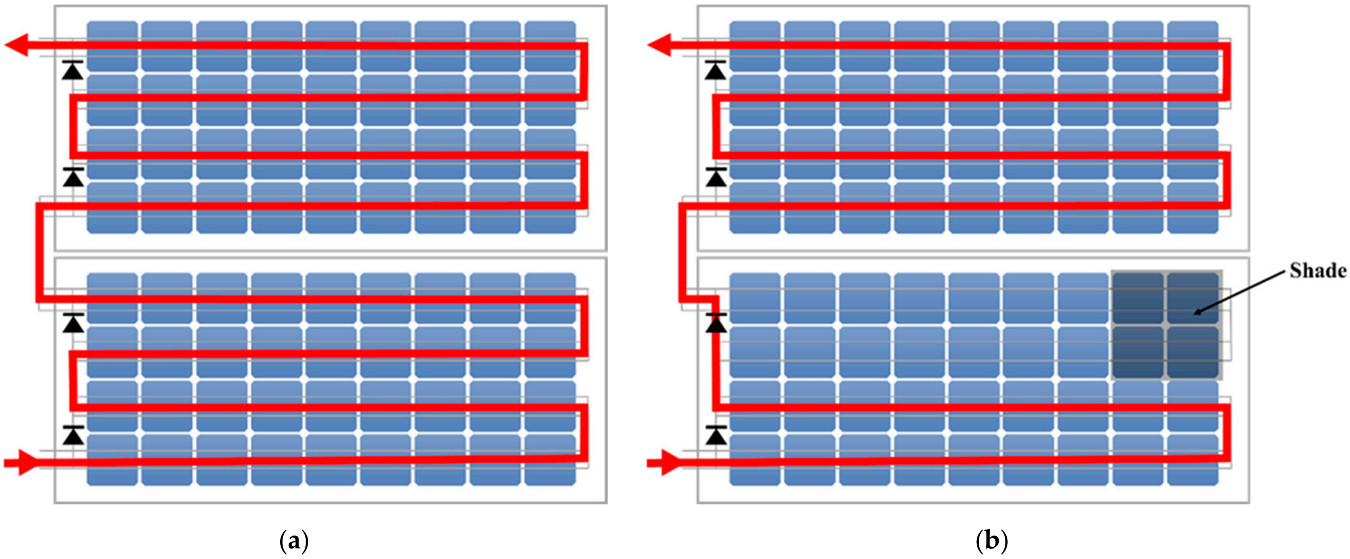

Figure 2. Schematic diagram of a solar cell module: (**a**) Normal power generation; (**b**) Bypass diode operation.

2.2. Photovoltaic Module Used in This Work

Figure 3 shows a single-crystal Si solar-cell module manufactured by KIS Co., Ltd., Osaka, Japan. This photovoltaic module uses 36 single-crystal Si cells (four vertical × nine horizontal cells) connected in series. The dimensions of the solar cells are 125 mm × 125 mm. Table 2 lists the module ratings.

Figure 3. The photovoltaic module used in this work.

Table 2. List of the rated values of the photovoltaic module used for this study.

Item	Output Value	Performance
Nominal maximum power (P_m)	90 (W)	>90%
Nominal maximum output operating current (I_{pm})	5.06 (A)	
Nominal maximum output operating voltage (V_{pm})	17.8 (V)	
Nominal short-circuit current (I_{sc})	5.4 (A)	>90%
Nominal open-circuit voltage (V_{oc})	22.4 (V)	±10%

Single-crystal Si solar cells are the most common type of solar cells and are used in several applications. In addition, they have a simple structure in which solar cells are connected in series, making it easy to distinguish between individual cells. Therefore, a single-crystal Si solar cell was used in the experiment.

Figure 4 shows a schematic diagram of the back side of the photovoltaic module. This module was used for the experiments, and the connections between the cells inside could be switched freely. Moreover, because all the electrodes are directed to the outside, the current and voltage can be measured for each internal cell.

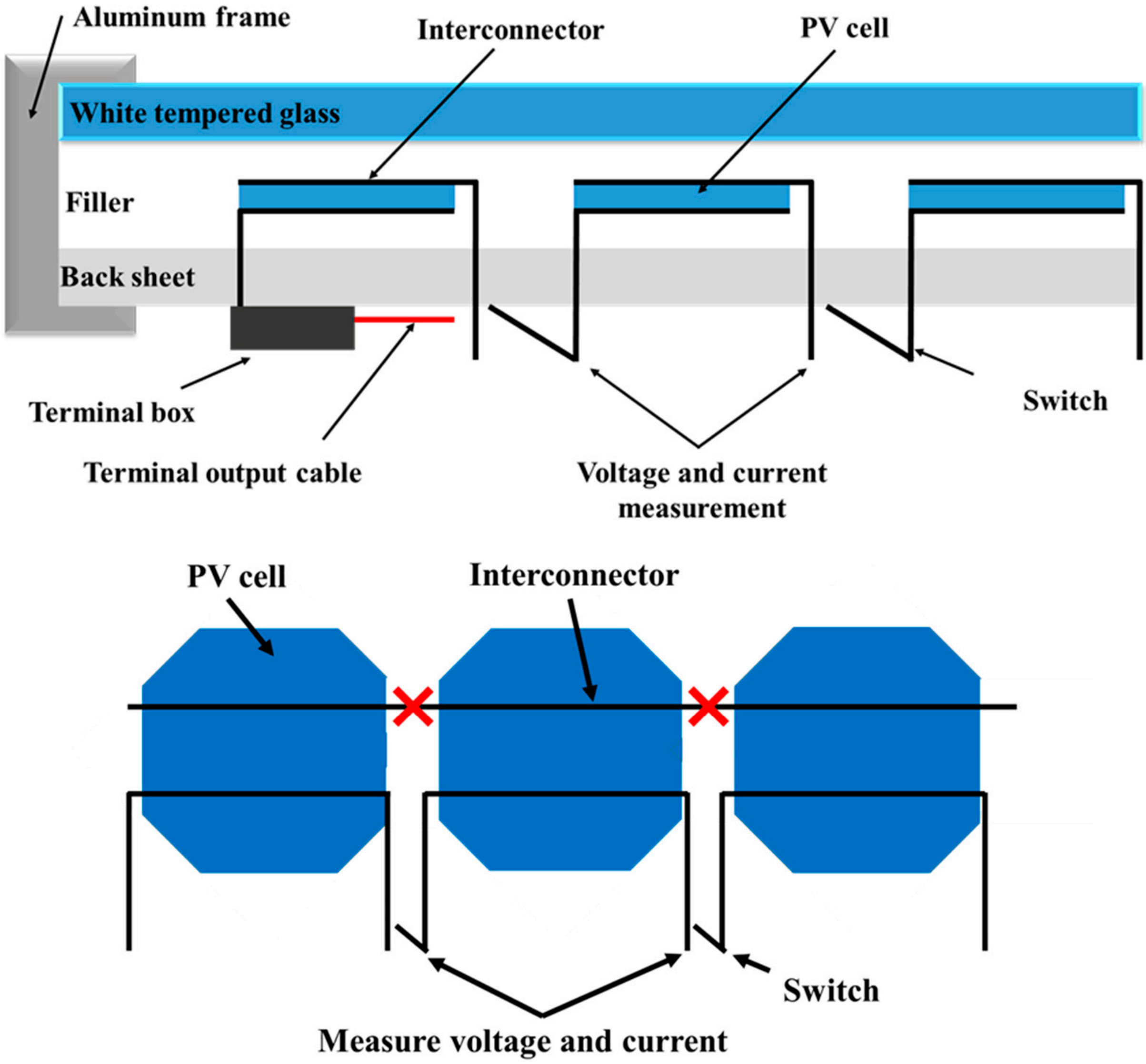

Figure 4. Schematic diagram of the backside of the photovoltaic module used for this work.

2.3. Testbed

To conduct the experiment indoors, we prepared a stand to install solar cells using an aluminum frame. An LED bulb was used as the light source. Figure 5 shows an LED bulb after processing. Because the irradiance of light from the LED light bulb is low in the commercially available state, the spherical plastic cover was cut in half. In addition, the directivity was improved by attaching aluminum tape to the plastic cover. Table 3 shows the relationship between the processing state of the LED bulb and irradiance. The irradiance of one LED bulb after processing increased by approximately 60 W/m^2 compared with the state without processing.

Figure 5. LED bulb (after processing).

Table 3. Relationship between processing state and irradiance of the LED light bulb.

Condition	Irradiance (W/m^2)
No processing	152.4
Cover cut	185.7
+Aluminum tape attached	218.5

The type of LED is a white-light light source with a color rendering index of 83. The range of the wavelength is 400 to 780 nm.

Figure 6 shows the layout of the LED bulb on the solar cell module. Six vertical and 11 horizontal LED bulbs were arranged so that the light-receiving surface of the solar cell module had as uniform an illuminance distribution as possible. The distance between the LED bulbs was set at 12.5 cm, and the length of one side of each cell was such that only one LED bulb was placed directly above each cell.

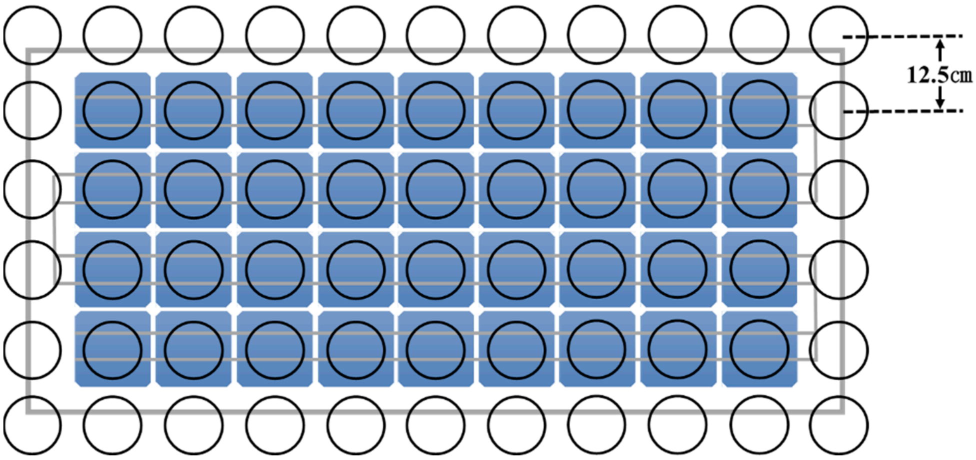

Figure 6. Layout of LED bulbs on solar modules.

Figure 7 shows the illuminance distribution on the glass surface of the solar-cell module. The sheer numbers (1 to 4) and horizontal numbers (1 to 9) in Figure 7 indicate the positions of the cells in the module. The average irradiance distribution on the glass surface was 401.8 W/m^2, the maximum irradiance was 418.6 W/m^2, and the minimum irradiance was 385.6 W/m^2. The LED bulb processing and multiple bulbs ensured a minimum outdoor irradiance of 200 W/m^2 in the MPPT system.

Average irradiance [W/m²]	Maximum irradiance [W/m²]	Minimum irradiance [W/m²]
401.8	418.6	385.6

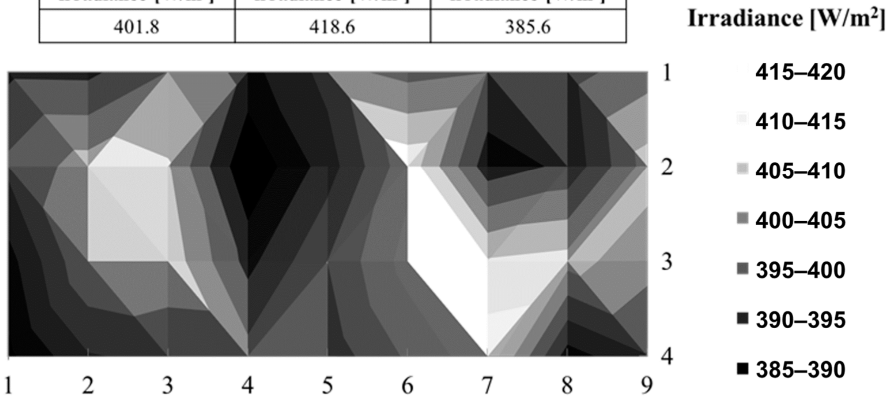

Figure 7. Irradiance distribution on the glass surface of the photovoltaic module.

2.4. Surface Potential Meter

In this experiment, a surface potential meter (TREK JAPAN Co., Ltd. Currently acquired by Advanced Energy Industries, Inc.) was used to measure the potential of the solar cell module [34]. A surface potential meter measured the potential from the reference potential on the surface. In general, when the surface of a substance is charged, it is challenging to measure the potential by contacting the tester because the amount of charge is small. However, because a surface potential meter converts the potential from the amount of charge induced on the detection electrode by the electric field, it is possible to measure the potential of the surface of the material without directly touching the object to be measured. Figure 8a shows the main body of the surface potential meter and Figure 8b shows the probe part. The surface potential meter is divided into a main body and a probe; the measured value is displayed on the main body, and the electrodes of the probe detect the electric field.

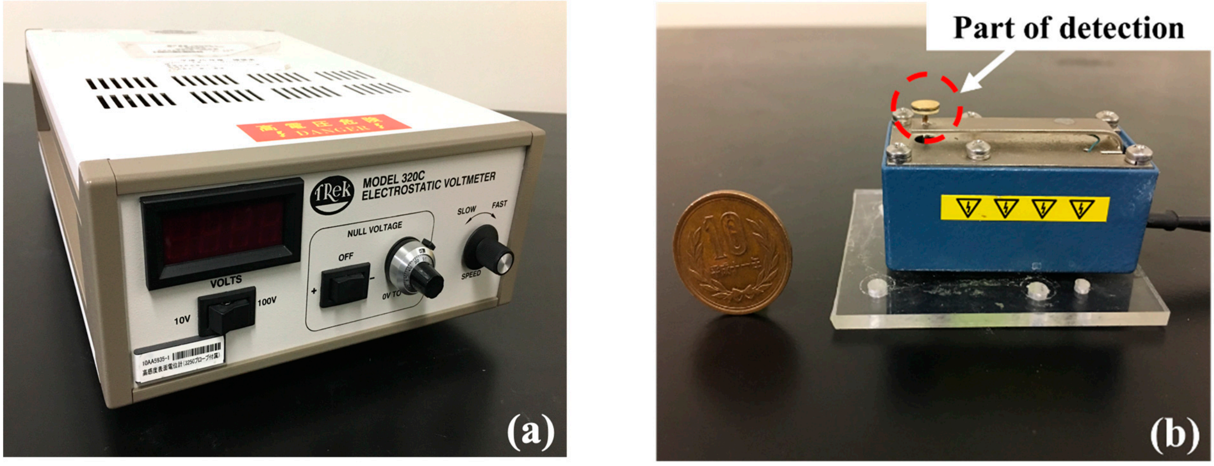

Figure 8. Surface potential meter: (**a**) Instrument body and (**b**) probe.

The measurement principle of the surface potential meter is explained here. Figure 9 shows a schematic diagram of the measurement principle of the surface potential meter. The principle of the non-contact potential measurement is based on electrostatic induction. For example, in Figure 9, because the charged object is negatively charged, positive charges gather near the charged object owing to the electric field of the detection electrode, and negative charges are driven away. At this time, a current flows through the resistor inside the surface potential meter according to the reference potential, generating a voltage across the resistor. The surface potential of the charged substance was determined using this voltage. Alternating this electric field with a mechanical chopper induced an AC-modulated signal in the electrodes. This alternating current signal was amplified and synchronously detected to reduce noise.

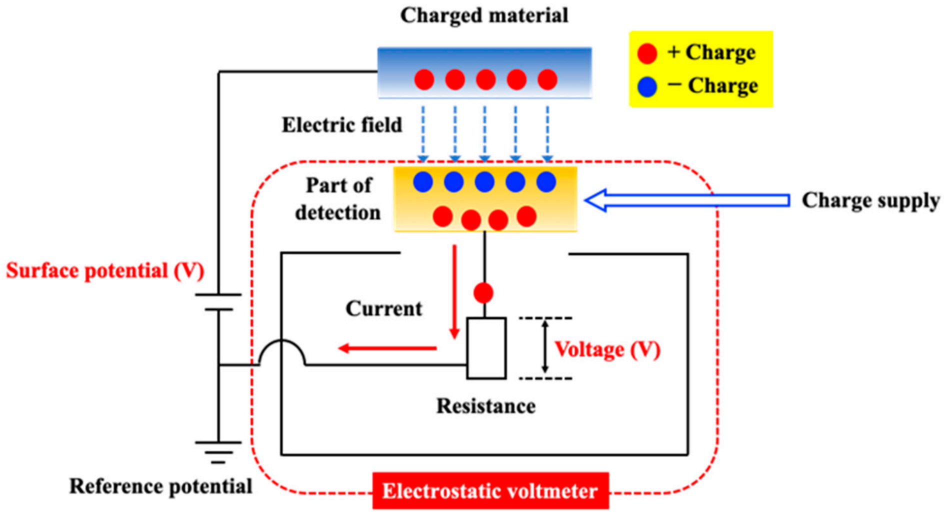

Figure 9. Schematic diagram of the measurement principle of a surface potential meter.

2.5. Pyranometer

A pyranometer (Eiko Seiki Co., Ltd., Tokyo, Japan) was used to measure the irradiance of the LED bulbs. Table 4 shows the ratings, and Figure 10 shows the pyranometer. The light-receiving part has no wavelength dependence and is coated with a unique black paint with absorption. Furthermore, the double glass structure renders it less susceptible to factors other than sunlight, such as wind and temperature changes.

Table 4. Ratings of the pyranometer.

Condition	Irradiance (W/m^2)
Response time	about 17 s
Viewing angle	2π (sr)
Operating temperature range	10 to +50 °C (accuracy guaranteed range) −40 to +80 °C (operating temperature range)
Temperature characteristics	±2% or less (rate of response change when ambient temperature changes by 50 °C)

Figure 10. A pyranometer used for this work.

2.6. Datalogger

In this experiment, a data logger was used to record the voltage, which was measured using a surface potential meter. Figure 11 shows the data logger, and Table 5 lists the functions of the data logger. In addition to freely setting the recording interval, multiple channels can simultaneously measure the voltage, temperature, and resistance.

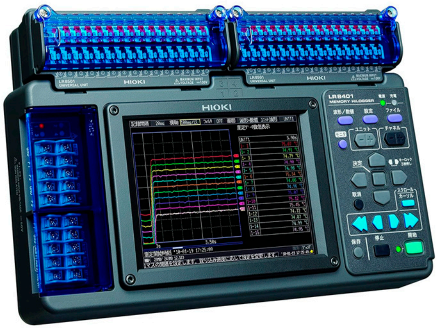

Figure 11. Data logger used for this work.

Table 5. Ratings of the data logger.

Condition	Values
Voltage measurement range	±1 mV to ±100 V 1–5 V
Resolution	500 nV
Recording interval	10 ms to 50 ms, 100 ms to 1 h
Dimensions	272 *W* × 182.4 *H* × 66.5 *D* mm
Functions	Real-time saving to USB memory, Numerical value/waveform calculation, etc.

2.7. Calculation Method of Potential Difference by Surface Potential Meter

This paper describes a method for calculating the potential difference of a solar cell module using a surface potential meter. When measuring the potential from the glass surface, we set the reference potential to the +terminal and set it to the −terminal when measuring the potential from the backsheet surface. The potential was measured from the backsheet surface during light reception and during light shielding. The potential difference owing to the presence or absence of light reception was calculated. Figure 12 shows the potential difference calculation method for each measurement surface. The number of cells inside the PV module from the terminal was set to the reference potential. Figure 12 shows the potential measurements of No. 2 cells on both surfaces. The potential difference calculated for the No. 2 cell was the integrated potential difference between the No. 1 and No. 2 cells when the internal cells were connected in series. Furthermore, the potential difference per No. 2 cell was obtained by subtracting the potential difference in the No. 1 cell from the potential difference in the No. 2 cell.

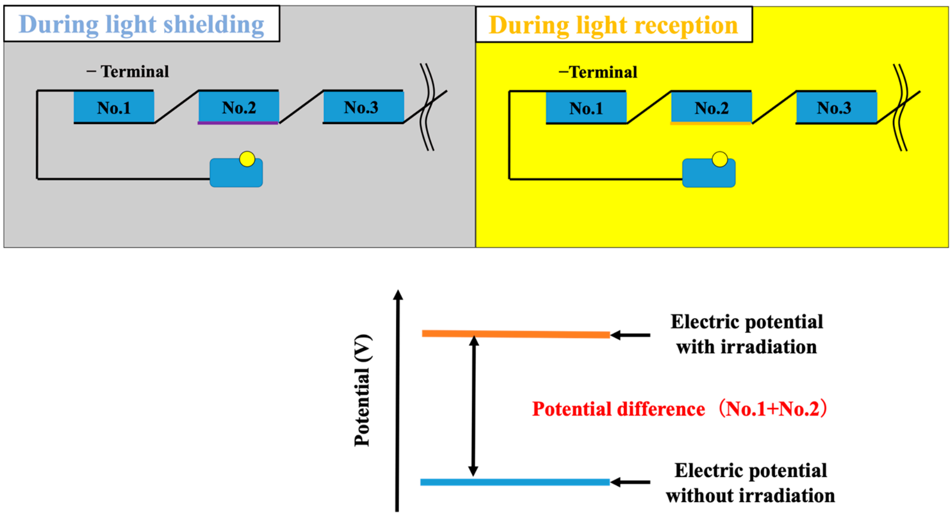

Figure 12. Measurement method for each measurement surface.

2.8. Experimental Method—General Procedure

We measured the potential of the PV module in three states: the open state, electronic load operating state, and short-circuited state, and we calculated the potential difference between the light receiving and light blocking in each cell. The potential difference and integrated voltage in each cell and the potential difference and voltage per cell were compared.

2.9. Experimental Method—Open Circuit Condition

Potential measurements were performed on both sides of the backsheet to verify the dependence on the measurement plane. Figure 13 shows the order of the potential measurements from the backsheet surface. The cells in the PV module were numbered in order from the negative terminal, which was used as the reference potential, and the potential was measured according to the order of the numbers. Subsequently, the potential difference and integrated voltage in each cell and the potential difference and voltage per cell were compared.

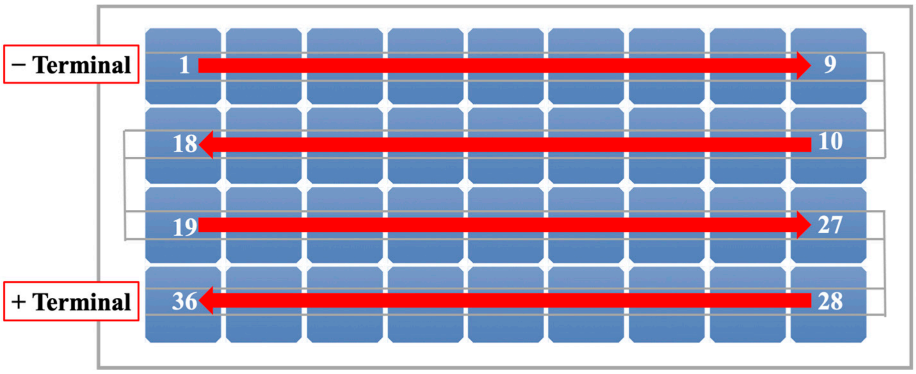

Figure 13. Order of potential measurements—Open circuit condition.

2.10. Experimental Method—Short Circuit Condition

The potential was measured by short-circuiting the PV module's positive and negative terminals. Figure 14 shows the sequence of the potential measurements. Additionally, potential measurements were performed for each cell from the backsheet surface of the PV module, and the potential difference was calculated. Furthermore, the potential difference and integrated voltage of each cell and the potential difference and voltage per cell were compared. Figure 15 shows a schematic diagram of the current measurements. All the cells in the PV module were disconnected, and the current of each cell was measured. Short-circuiting PV modules may experience voltage drops in low-current cells. Therefore, we verified whether the cell in which the voltage drop occurred matched the low-current cell.

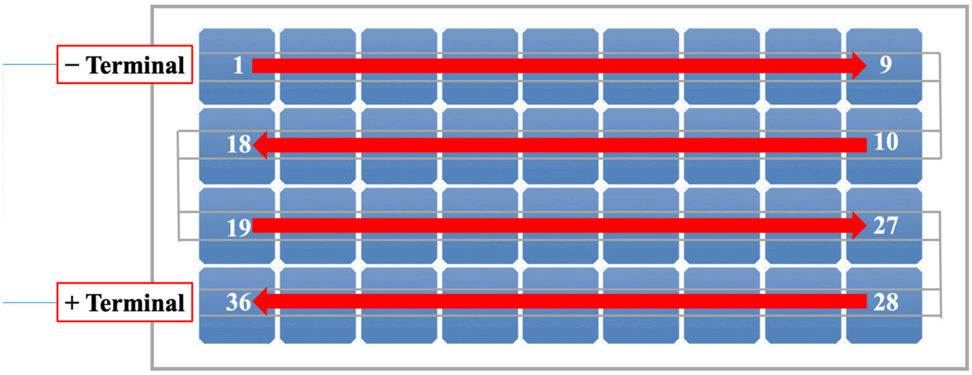

Figure 14. Order of potential measurements—short circuit condition.

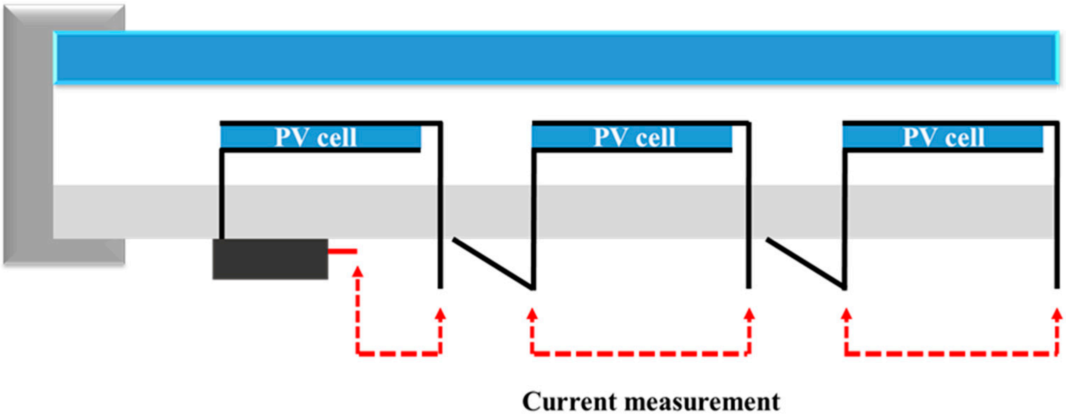

Figure 15. Schematic diagram of the current measurement.

Next, based on the results of the above current measurement, the cell with the largest current was shielded, and the potential difference, voltage, and current per cell were measured. Thus, the relationship between the current value and the cell in which the voltage drop occurred and the relationship between the shielding area and the magnitude of the voltage drop were verified. Figure 16 shows a schematic of the shielding process. The shielded area was changed 10 times (1–10%) with respect to the area of the cell.

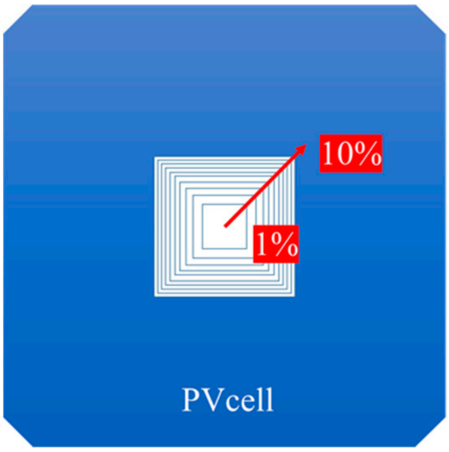

Figure 16. Schematic diagram of the shielding situation.

2.11. Procedure for the Risk Assessment of Fire Hazards

This method measures the reverse-bias voltage caused by the current mismatch. The flowchart of the assessment of the fire risk is shown in Figure 17. The fire risk caused by the reverse-bias voltage was well researched to the typical crystalline Si solar cells, and the criterion was known as −13 V [37–39]. Otherwise, the quantified estimation of the fire risk will be assessed by estimating the maximum temperature of the worst-case environment. First, the heat dissipation of the reverse-biased solar cell is calculated by the product of the reverse-bias voltage and worst-case cell current. With the value of heat dissipation, the maximum temperature will be estimated considering the worst case. It is proportional to the heat dissipation, and the Si cells' coefficient is 280 $\mathrm{Kcm^2/W}$ [38]. If the maximum temperature exceeds the firing point, it will be assessed as the risk of fire.

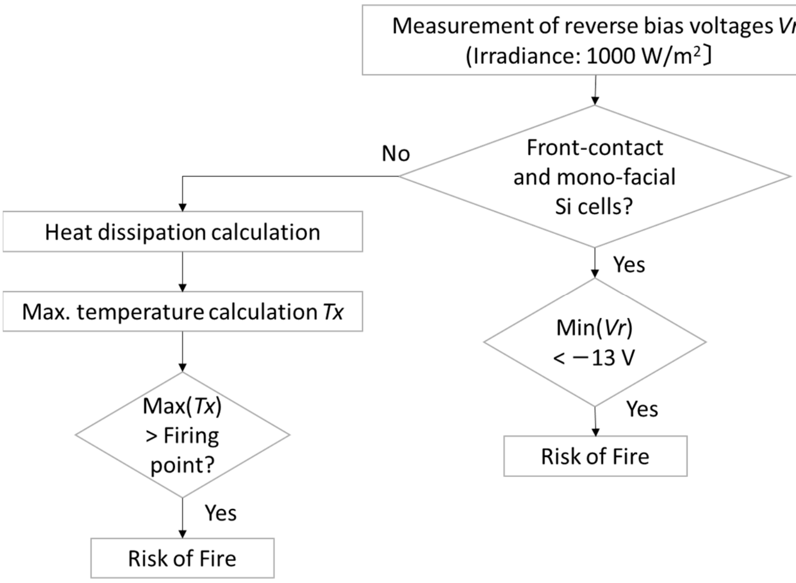

Figure 17. Proposed flowchart of detection of the fire risk in this work.

3. Results

3.1. Photovoltaic Module in the Open-Circuit Condition

Figure 18 shows the potential difference and integrated voltage in each cell measured from the backsheet surface. Figure 19 shows the potential difference and voltage per cell measured from the backsheet surface. The potential difference and integrated voltage measured in each cell increased with the number of cells. The potential difference in the No. 36 cell, which was the reference potential and furthest from the negative terminal, agreed with the open-circuit voltage Voc of the PV module with a small error. The change in the potential difference between the cells was calculated. Compared with the voltage of each cell measured by the tester, it matched with a slight error of 0.1 V. The potential difference in the cell farthest from the terminal, used as the reference potential, corresponded to the voltage of the entire PV module, and the potential difference per cell corresponded to the voltage of each cell.

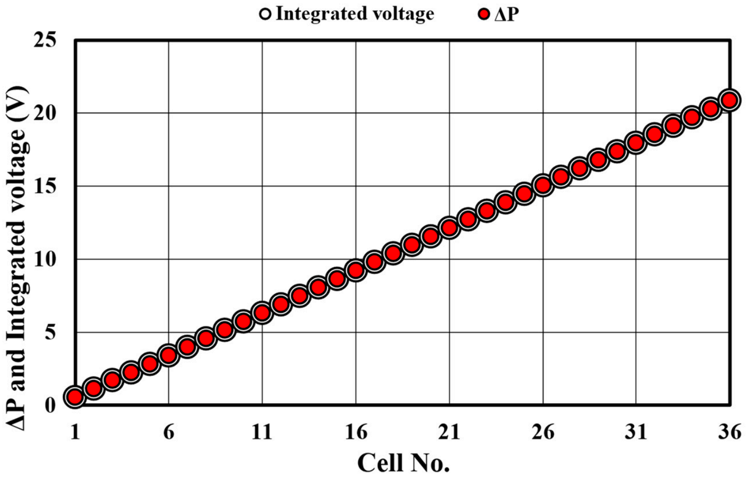

Figure 18. Potential difference and integrated voltage in each cell (backsheet surface).

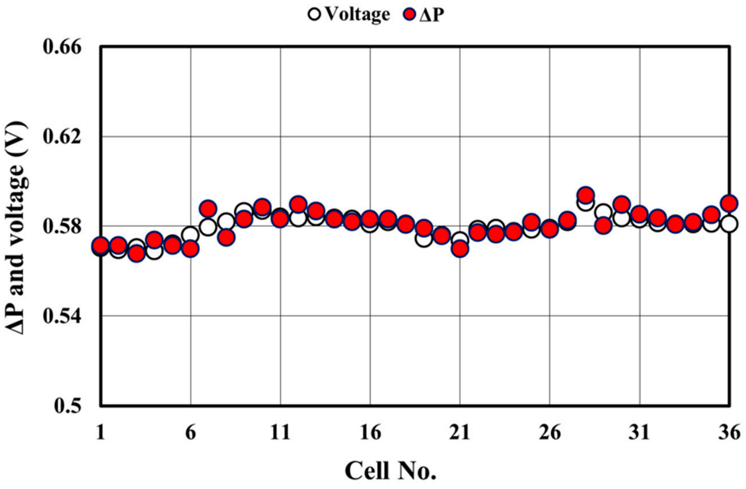

Figure 19. Potential difference and voltage per cell (backsheet surface).

The total voltage read by Figure 18 was 20.9 V, and the rated open-circuit voltage was 22.4 V (10% error). The lower measured voltage was due to illumination irradiance (400 W/m^2) being less than the standard testing condition. After correction by the irradiance, the calculated rated voltage will be (22.4 V) + (0.027 V) × ln (0.4) × 36 = 21.5 V, and it is close to the measured value of 20.9 V within 10% of the measurement error.

The direct voltage measurement validated the measurement error (Figures 18 and 19), which was as small as we expected, as specified in Section 2.4. Note that the contact distance is substantially smaller than the solar cells' size, and the electrical field is almost vertical to the module surface, so the detected voltage can be estimated by 1D arithmetic calculation in Section 2.4. The measurement error and reproducibility are also discussed in Section 4.1. The error range found in Figure 19 was in the order of 0.01 V, but the one in Figure 20 was in the order of 0.1 V. These errors corresponded to the resolution of the instruments varied by the range of the voltage, namely, 0.1 V in the 100 V range and 0.01 V in the 10 V range.

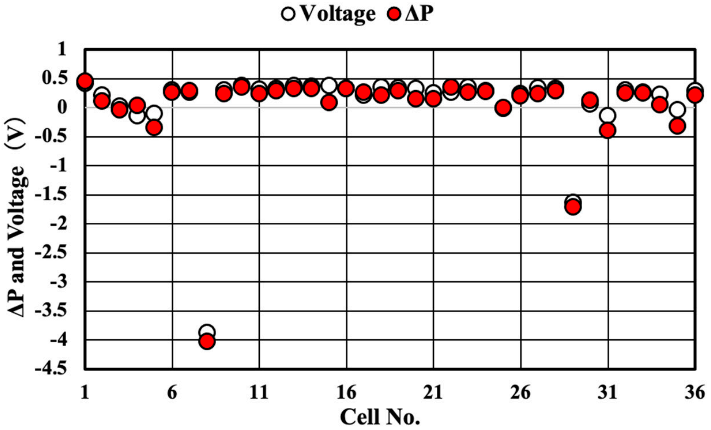

Figure 20. Potential difference and voltage per cell (short circuit).

3.2. Photovoltaic Module in the Short-Circuited Condition

Figure 20 shows the potential difference and voltage for each cell. Significant voltage drops occurred in the No. 8 and 29 cells. Figure 21 shows the current in each cell. The current values of the No. 8 and 29 cells tended to be lower than those of the surrounding cells. In addition, this cell coincided with the cell in which the voltage drop occurred, as shown in Figure 20. In a short-circuited PV module, the voltage of each cell is consumed within the module. The internal cells of the PV module used in this experiment were connected in series. Therefore, it is considered that the low-current cells inside the PV module act as a resistance, causing a voltage drop.

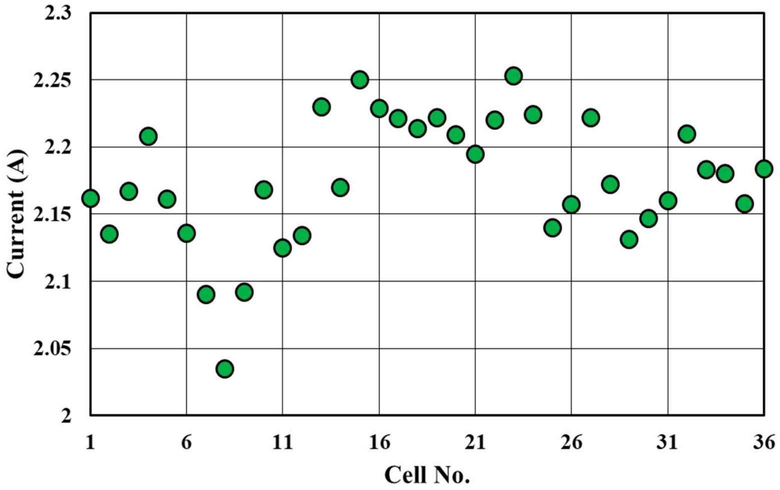

Figure 21. The current of each cell (short-circuited, and each cell was disconnected from a series connection circuit).

For the difference of cells No. 8 and No. 29 from other cells in the module, we believe it was due to imperfection. We did not give any intentional damage. However, it was known that the PERC cell or other single-crystalline solar cells sometimes show a conchoidal EL pattern after applying a substantial reverse-bias voltage. This suggests that significant mismatching conditions and reverse voltage stress would damage the solar cells. Therefore, we cannot deny that the stress damaged the solar cells in that module during our experiments.

Figure 22 shows the voltage before shielding, and Figure 23 shows the current value. As shown in Figure 23, the No. 15 cell exhibited a higher current value than the other cells. Therefore, the No. 15 cell was shielded, and the current and voltage per cell were measured in each shielded area (1–10%). Figure 24 shows the voltage per cell for each shaded area (1–10%). Figure 24 shows that no voltage drop occurred when the No. 8 cell was not shielded. However, a voltage drop occurred when the shielded area was 9–10%. In addition, by shielding the No. 15 cell, the voltage drop in the No. 8 cell decreased. Figure 24 shows the voltage per cell for the No. 8 and No. 15 cells in each shielding area, and Figure 25 shows the current. From Figure 24, when the shielded area is 9% or more of the area of one cell, a voltage drop of −4 V or more occurs.

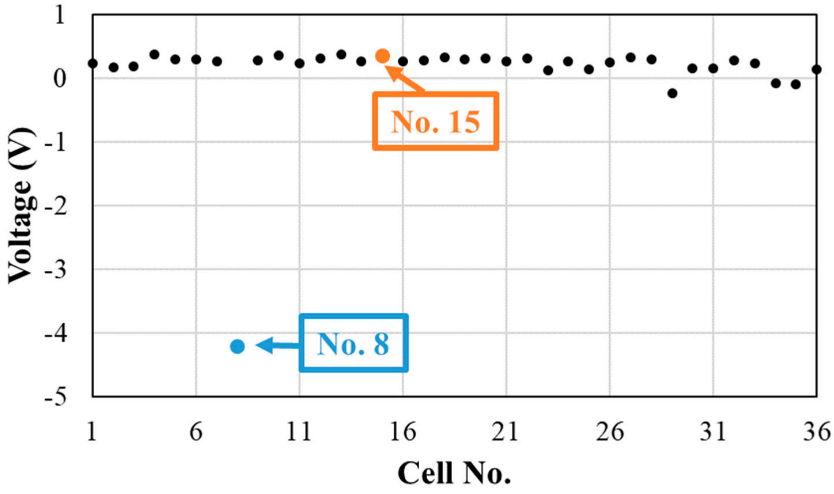

Figure 22. The voltage of each cell before shielding.

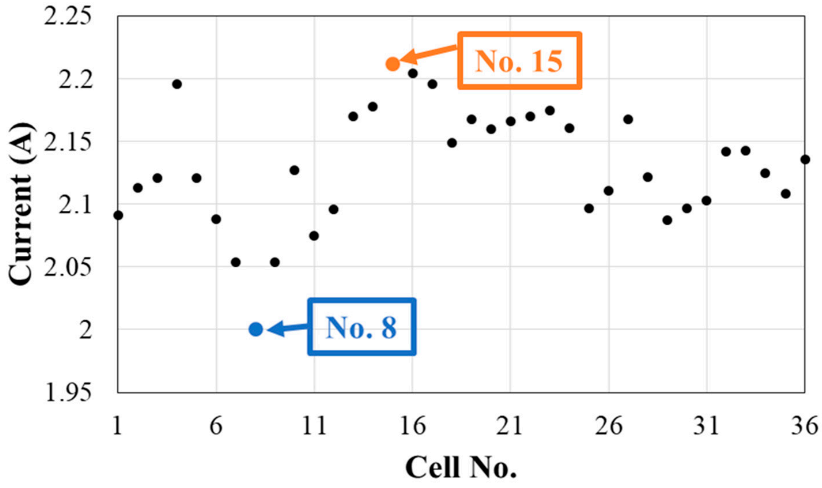

Figure 23. The current of each cell before shielding.

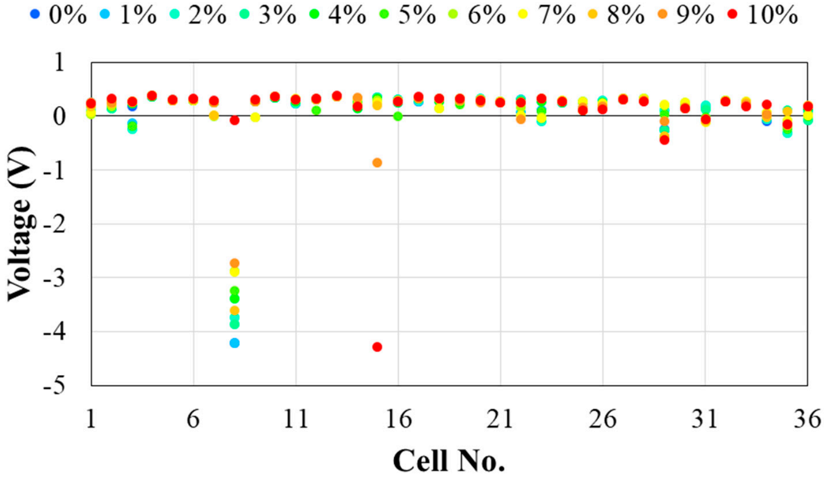

Figure 24. Voltage per cell at each shaded area (1–10%).

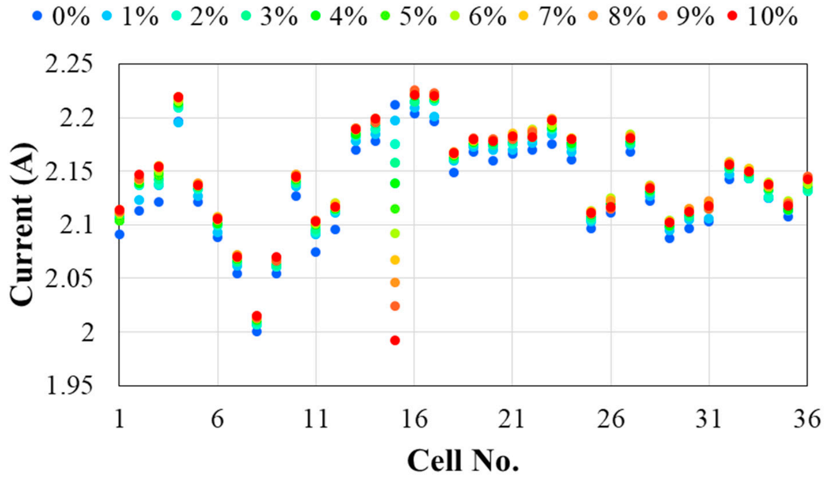

Figure 25. Current per cell at each shaded area (1–10%).

Figure 26 shows the current values of the No. 8 and No. 15 cells in each shielding area. Because the light-receiving area of the cell and the current have a proportional relationship, the current decreased as the shielding area increased in the No. 15 cell. In addition, when the current value of the shielded No. 15 cell fell below the current value of the No. 8

degraded cell, a voltage drop occurred in the No. 8 cell. Thus, among the cells connected in series inside the PV module, a voltage drop occurred in the low-current cell, and the magnitude of the voltage drop was determined by the difference in the current value from the other cells.

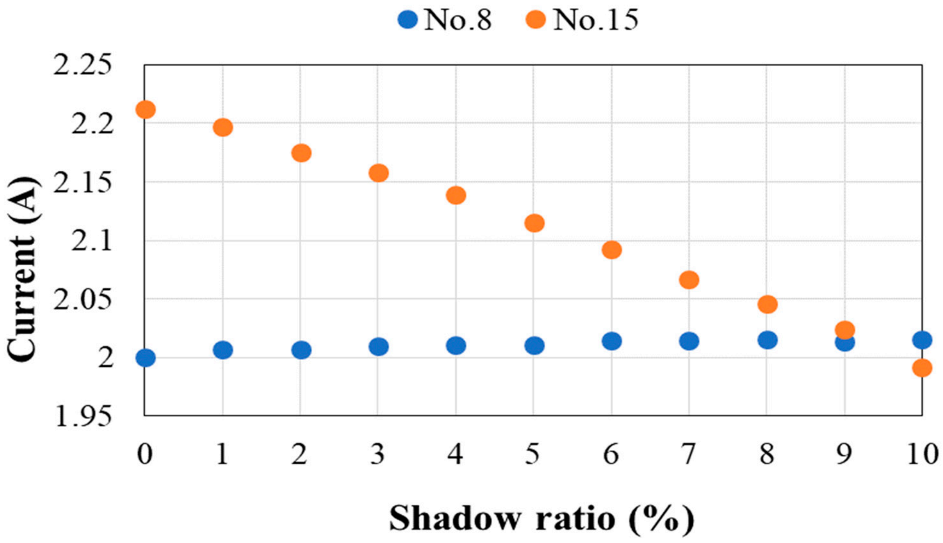

Figure 26. The current of the No. 8 and No. 15 cells in each shaded area.

Cells with degraded performance showed a slight current drop but a significant voltage drop.

It is known that the high absolute value of the reverse-bias voltage of each cell causes hot-spot failure and leads to local temperature rise, and its criterion is also known as minus 13 V [37–39]. Our examination of demonstration in the detection and reproducibility of reverse-bias voltage was carried out using a commercial photovoltaic module (thus, the quality of each solar cell was assumed to be good) without degradation. Even the worst reverse-bias voltage by the worst solar cell was −4.3 V (average irradiance: 401.8 W/m^2 and assumed −10.8 V under 1000 W/m^2 irradiance before surrendering to the reverse-bias voltage). However, the detection capability and voltage reproducibility were validated. We believe this non-contact inspection method helps assess fire risk for the modules assumed to be degraded.

4. Discussion

4.1. Reverse-Bias Voltage Measurement

In this study, we verified a highly accurate voltage calculation method for PV modules and element cells in PV modules based on non-contact potential measurements using surface voltmeters. Using this method, we investigated a method for detecting degraded cells in PV modules.

The open-circuit voltage Voc of the PV module in the open state, the potential difference of the No. 36 cell, and the potential difference and voltage per element cell were compared. Thus, from both the glass surface and the backsheet surface, the potential difference and open-circuit voltage Voc of the No. 36 cell and the potential difference and voltage per cell matched with a small error. In addition, the potential difference and voltage per cell agreed at ±0.1 V. Therefore, it is effective for monitoring the operating conditions of each solar cell in the PV modules without contact.

The PV modules under short-circuited conditions experienced voltage drops in the internal low-current cells. Although the difference in the current value between the low-current cell and the other cells was minimal, a clear difference appeared in the voltage per cell. Therefore, when the potential difference per cell and voltage match, it is possible to identify low-performance cells in the PV module. However, the maximum error increased to 0.3 V due of the decreased irradiance of the LED bulb used as the light source. Therefore, if the potentials of all the cells can be measured simultaneously in a uniform illuminance distribution, a more precise detection of performance differences can be expected.

One of the interests in applying this method for inspecting the module outside (on the roof of houses or the rack of the solar power plants) is that solar irradiance is not always 1000 W/m^2. A question arose: How to correct the measured reverse-bias voltage corresponding to the solar irradiance level in the field? The reverse-bias voltage is the $V_{pm} - (I_{pm0} - I_{pm})R_{sh}$, or $V_{oc} - (I_{sc0} - I_{sc})R_{sh}$, depending on the load resistance, and before the junction does not reach (partial) breakdown. The correction of the V_{pm} and V_{oc} are approximated as adding the equivalent voltage of ln(ratio of the solar irradiance to the standard value of 1000 W/m^2) × (0.027 V). The correction of all the current parameters is proportional to the solar irradiance to the standard value of 1000 W/m^2.

Another practical question is the impact of the bypass diodes. The number of diodes in the module is usually three and includes 20 or 24 solar cells (depending on the module with 60 or 72 cells). There are also three diodes in the half-cut cell modules, but three series strings comprise two groups of parallel half-cut cells. A question is if a difference in configuration affects the measurement.

The function of this Inspection is to estimate a reverse-bias voltage caused by current mismatching of the module. The reverse-bias voltage is the $V_{pm} - (I_{pm0} - I_{pm})R_{sh}$, or $V_{oc} - (I_{sc0} - I_{sc})R_{sh}$, depending on the load resistance, and before the junction does not reach (partial) breakdown. We measured it under short-circuit conditions so that the second formula will be applied. I_{pm0} and I_{sc0} are normal I_{pm} and I_{sc}. The function of the bypass diodes to the circuit behavior is to clip the I_{sc} to I_{sc0}. Nevertheless, the number of bypass diodes is the detected reverse-bias voltage of the degraded solar cell, and the current mismatching will be the same.

4.2. Accuracy and Reproducibility of Reverse-Bias Voltage

The distance from the probe needle to the solar cell surface should be controlled for accurate and reproducible measurements. The non-contact distance is crucial to the measurement. With an increase in the distance, the detected voltage drops. The maximum distance can be estimated by electromagnetics calculation. First, the surface of the module's cover glass (3.3 mm thick) with a relative permittivity of 5.4, and lamination resin (EVA, 0.45 mm thick) with a relative permittivity of 2.6, gives a distance of 3.75 mm. The weighted harmonic average can calculate the measured voltage drop per unit length, and it is 4.78 (=((3.75 mm)/((3.3 mm)/5.4 + (0.45 mm)/2.6))). Namely, if 0.2 V of the error by the difference of the distance is accepted (average voltage was 0.58 V as shown in Figure 18), the acceptable distance from the surface of the glass is (0.2 V)/(0.58 V) × (3.75 mm)/4.78 = 0.27 mm. In this experiment, we set the total distance as 4 mm (=3.75 mm + 0.27 mm = 4.02 mm).

Another crucial parameter is the resolution of the voltage, namely sensitivity to the number of electrical carriers that move during the measurements. The instrument we used specifies 0.1 V of resolution. It is a considerably small value for the detection of fire risk. Since the typical hot-spot power dissipation is 0.53 W/cm^2 for the temperature of 220 °C, and for 250 cm^2 (156 mm × 156 mm) solar cells with 9 A output current solar cells (40 mA/cm^2 current density), the corresponding voltage of the solar cell with fire risk will be 0.53 W/cm^2/32 mA/cm^2 = 13.3 V, which is substantial enough to the specified resolution of 0.1 V. Also note that −13 V is known as the maximum reverse-bias voltage for Si solar cells that may lead to hot-spot problems [37–39].

4.3. Calculation on Temperature Rise to Assess Fire Risk

The above non-contact method is also helpful in anticipating how much local loss in specific solar cells under given operating conditions leads to a local temperature rise, which is responsible for fires. It is also helpful to detect symptoms of infant degradation, potentially leading to fires caused by partial shading (leading to hot spots) and whether this local temperature rise exceeds the firing point. The magnitude of the local heat source is calculated using the following equation:

$$\text{(local heat source)} = -\text{(current at the string)} \times \text{(surface potential voltage)}$$

Note that the surface potential varies according to the operating conditions, such as the degree of partial shading and solar irradiance. The standard surface potential value is positive, typically 0.6 V for Si solar cells. However, the cell creates a hot spot, resulting in a negative and much more significant absolute surface potential value.

It is also helpful for non-destructively evaluating the performance variation of solar cells in a PV module. Given uniform illumination by an artificial light source and measurement of the surface potential in each solar cell, the surface potential variation corresponds to the variation in the output current potential (short-circuit current of the solar cell when independently measured). Specifically, the detected reverse voltage indicates that the solar cell has a lower short-circuit current than the cells of the other modules.

Since it detects electrical fields from individual cells, it can only be applied to the modules with explicitly separate cells and not used like amorphas modules. Although the principle of the fire risk is the same given the temperature rise of the solar cells induced by the reverse-bias voltage, the impact of the hot-spot creation leading to the fire hazards varies by the type of modules [36,40–43], including even the difference of the cell structure in single-crystalline solar cell family [36]. This work investigated the non-contact and non-destruction inspection of the reverse current voltage of each cell in the module, and it is common to every type. However, the criteria may vary among types of solar cells and modules. For example, that of the Perovskite solar cells may be −9 V [43]. The impact of efficiency difference also affects the criterion through the term of the operating temperature of the solar cell under the worst-case solar irradiance.

4.4. Variation by the Type of Solar Cells and Module Configuration

The acceptable reverse-bias voltage for crystalline Si solar cells was studied intensively and agreed upon −13 V [37–39]. However, it may not be consistent with other types of solar cells, like −9 V in Perovskite solar cells [42]. However, some back-contact solar cell (IBC cell) claims that the lower hot-spot temperature was also reported due to lower reverse-bias voltage [36,44]. We think a parasitic Zener diode caused it to act like a bypass diode in the islanded junctions at the back contact. We also observed the same types of behavior at MWT back contact solar cells. Also, it was reported that the reverse-bias voltage tended to slightly increase by the solar cells with higher efficiency [36]. Therefore, relying on a single criterion of −13 V may be more dangerous for back-contact solar cells and other types of cells than crystalline Si cells.

Also, it is not applied to the bifacial modules, since the output current in mismatching conditions may be expanded to 1.35 times [40]. Still, the measurement of the reverse-bias voltage (non-contact and non-destructive measurement in this work) is effective for assessing the fire risk by calculating the local heat dissipation in the solar cell and the maximum temperature.

5. Conclusions

We proposed a non-contact diagnostic method for the local reverse voltage caused by partial shading and mismatch loss using surface potential meters. We expect this method to help prevent fires from PV modules and detect degraded or underperforming solar cells inside the PV module using non-contact and non-destructive methods.

For the assessment of the fire risk, the following contributions were made by this work.

- ♦ We developed a non-contact measurement method by detecting the carrier movement by the electrical field generated by the surface potential of the solar cell inside the module (in between the cover glass and the back sheet). The heat dissipation of the solar cell leading to a fire hazard is quantitatively calculated by the product of the circuit current and the detected reverse-bias voltage.

- The above method was validated by measuring each cell's reverse-bias voltage without cutting the circuit in the module. The error range was sufficiently small for the fire risk assessment.
- Demonstration of the fire-risk assessment by the non-contact measurement by the following steps:
    1. Non-contact measurement of the reverse-bias voltage under the controlled operating condition.
    2. Calculate each solar cell's heat dissipation per area (W/cm^2) by multiplying the reverse-bias voltage and output current by the load resistance.
    3. Estimation of the maximum temperature of each cell under a given condition. The worst-case solar irradiance may be 1400 W/m^2, and the maximum temperature is proportional to the solar irradiance level. The typical calculation of the worst-case temperature with typical values follows: (261 °C: Worst-case temperature) = (13 V: Reverse-bias voltage tested at 1000 W/m^2) × (38 mA/cm^2: Short-circuit current density of the cells per area, under standard testing condition, 1000 W/m^2) × (280 Kcm^2/W: Temperature rise per unit heat dissipation) × (1.38: Current correction on solar irradiance correction for the worst-case) + (70 °C: Operating temperature of the solar cell under worst-case solar irradiance) > (250 °C: Firing point of woods)

In this case, the photovoltaic module under inspection is categorized as "Risk of fire".

In other words, a typical criterion of the maximum reverse-current voltage in the photovoltaic module to avoid fire risk is "−13 V," which is almost the same level as the maximum acceptable reverse-bias voltage of silicon solar cells, which are typically known as "−13 V" [37–39] given the international standards of IEC61215 [45] and IEC6173 [46]. In the current technology, the screening of the solar cells in the maximum reverse-bias voltage was inspected at the cell level before assembling the photovoltaic module. The reverse-bias voltage of each cell is not monitored or inspected after the module assembly due to the lack of non-contacting technology of the reverse-bias voltages, even when some cells are degraded. The innovative approach to this work is the inspection applicable after the assembly of the module and after installation and operation.

Note that we have not intensively examined the reproducibility as the fire assessment but only show the possibility of an innovative non-contact and non-destructive assessment of the fire risk. We believe this method will be a standard method after intensive examination of the reproducibility, like blind tests by testing laboratories.

Author Contributions: Conceptualization, K.N.; validation, R.S., Y.O. and A.N.; writing—original draft preparation, R.S.; writing—review and editing, K.A.; supervision, K.N. All authors have read and agreed to the published version of the manuscript.

Funding: This study received no external funding.

Institutional Review Board Statement: Not applicable.

Informed Consent Statement: Not applicable.

Data Availability Statement: Data will be made available on request.

Acknowledgments: We thank Yoshihiro Hishikawa at Ritsumeikan University for fruitful discussions on surface potential measurement technology.

Conflicts of Interest: The authors declare no conflict of interest.

References

1. 2018—Japa's Energy Problems. Available online: http://www.enecho.meti.go.jp/about/special/johoteikyo/energyissue2018.html (accessed on 4 July 2023).
2. BP Statistical Review of World Energy. 2016. Available online: https://www.bp.com/content/dam/bp/business-sites/en/global/corporate/pdfs/news-and-insights/speeches/bp-statistical-review-of-world-energy-2016-spencer-dale-presentation.pdf (accessed on 4 July 2023).
3. Ayompe, L.M.; Duffy, A.; McCormack, S.J.; Conlon, M. Measured performance of a 1.72-kW rooftop grid connected photovoltaic system in Ireland. *Energy Convers. Manag.* **2011**, *52*, 816–825. [CrossRef]
4. Myong, S.Y.; Park, Y.C.; Jeon, S.W. Performance of Si-based PV rooftop systems operated under distinct four seasons. *Renew. Energy* **2015**, *81*, 482–489. [CrossRef]
5. Razykov, T.M.; Ferekides, C.S.; Morel, D.; Stefanakos, E.; Ullal, H.S.; Upadhyaya, H.M. Solar photovoltaic electricity: Current status and future prospects. *Sol. Energy* **2011**, *85*, 1580–1608. [CrossRef]
6. Kazmerski, L.L. Photovoltaics: A review of cell and module technologies. *Renew. Sustain. Energy Rev.* **1997**, *1*, 71–170. [CrossRef]
7. Kumar, A.; Kumar, K.; Kaushik, N.; Sharma, S.; Mishra, S. Renewable energy in India: Current status and future potentials. *Renew. Sustain. Energy Rev.* **2010**, *14*, 2434–2442. [CrossRef]
8. Hart, E.K.; Jacobson, M.Z. A Monte Carlo approach to generator portfolio planning and carbon emissions assessments of systems with large penetrations of variable renewables. *Renew. Energy* **2011**, *36*, 2278–2286. [CrossRef]
9. Aliprandi, F.; Stoppato, A.; Mirandola, A. Estimating CO_2 emissions reduction from renewable energy use in Italy. *Renew. Energy* **2016**, *96*, 220–232. [CrossRef]
10. Sharma, V.; Chandel, S.S. Performance and degradation analysis for long term reliability of solar photovoltaic systems: A review. *Renew. Sustain. Energy Rev.* **2013**, *27*, 753–767. [CrossRef]
11. Emery, K.; Osterwald, C. Measurement of photovoltaic device current as a function of voltage, temperature, intensity and spectrum. *Sol. Cells* **1987**, *21*, 313–327. [CrossRef]
12. Dirnberger, D.; Kräling, U.; Müllejans, H.; Salis, E.; Emery, K.; Hishikawa, Y.; Kiefer, K. Progress in photovoltaic module calibration: Results of a worldwide intercomparison between four reference laboratories. *Meas. Sci. Technol.* **2014**, *25*, 105005. [CrossRef]
13. Munoz, M.A.; Alonso-García, M.C.; Vela, N.; Chenlo, F. Early degradation of silicon PV modules and guaranty conditions. *Sol. Energy* **2011**, *85*, 2264–2274. [CrossRef]
14. Alonsogarcia, M.C.; Ruiz, J.M.; Chenlo, F. Experimental study of mismatch and shading effects in the—Characteristic of a photovoltaic module. *Sol. Energy Mater. Sol. Cells* **2006**, *90*, 329–340. [CrossRef]
15. Wang, J.C.; Su, Y.L.; Shieh, J.C.; Jiang, J.A. High-accuracy maximum power point estimation for photovoltaic arrays. *Sol. Energy Mater. Sol. Cells* **2011**, *95*, 843–851. [CrossRef]
16. Verma, D.; Nema, S.; Shandilya, A.M.; Dash, S.K. Maximum power point tracking (MPPT) techniques: Recapitulation in solar photovoltaic systems. *Renew. Sustain. Energy Rev.* **2016**, *54*, 1018–1034. [CrossRef]
17. Breitenstein, O.; Bauer, J.; Bothe, K.; Hinken, D.; Müller, J.; Kwapil, W.; Schubert, M.C.; Warta, W. Luminescence imaging versus lock-in thermography on solar cells and wafers. In Proceedings of the 26th European Photovoltaic Solar Energy Conference and Exhibition, Hamburg, Germany, 5–9 September 2011; Volume 1.
18. Juarez-Lopez, J.M.; Franco, J.A.; Hernandez-Escobedo, Q.; Muñoz-Rodríguez, D.; Perea-Moreno, A.-J. Analysis of a novel proposal using temperature and efficiency to prevent fires in photovoltaic energy systems. *Fire* **2023**, *6*, 196. [CrossRef]
19. Aram, M.; Zhang, X.; Qi, D.; Ko, Y. A state-of-the-art review of fire safety of photovoltaic systems in buildings. *J. Cleaner Prod.* **2021**, *308*, 127239. [CrossRef]
20. Ravindra, N.; Lin, L.; Bora, B.; Prasad, B.; Sastry, O.; Mondal, S. Influence of outdoor conditions on PV module performance—An overview. *Mater. Sci. Eng. Int. J.* **2023**, *7*, 88–101. [CrossRef]
21. Cipriani, G.; D'Amico, A.; Guarino, S.; Manno, D.; Traverso, M.; Di Dio, V. Convolutional Neural Network for Dust and Hotspot Classification in PV Modules. *Energies* **2020**, *13*, 6357. [CrossRef]
22. Goudelis, G.; Lazaridis, P.I.; Dhimish, M. A review of models for photovoltaic crack and hot-spot prediction. *Energies* **2022**, *15*, 4303. [CrossRef]
23. Niazi, K.A.K.; Akhtar, W.; Khan, H.A.; Yang, Y.; Athar, S. Hot-spot diagnosis for solar photovoltaic modules using aIe Bayes classifier. *Sol. Energy* **2019**, *190*, 34–43. [CrossRef]
24. Dhimish, M.; Tyrrell, A.M. Power loss and hot-spot analysis for photovoltaic modules affected by potential induced degradation. *npj Mater. Degrad.* **2022**, *6*, 11. [CrossRef]
25. Bharadwaj, P.; Karnataki, K.; John, V. Formation of hot-spots on healthy PV modules and their effect on output performance. In Proceedings of the 2018 IEEE 7th World Conference on Photovoltaic Energy Conversion (WCPEC) (A Joint Conference of 45th IEEE PVSC, 28th PVSEC & 34th EU PVSEC), Waikoloa, HI, USA, 10–15 June 2018; pp. 676–680. [CrossRef]
26. Yuan, Z.; Xiong, G.; Fu, X. Artificial Neural Network for Fault Diagnosis of Solar Photovoltaic Systems: A survey. *Energies* **2022**, *15*, 8693. [CrossRef]
27. Parikh, H.R.; Buratti, Y.; Spataru, S.; Villebro, F.; Reis Benatto, G.A.D.; Poulsen, P.B.; Wendlandt, S.; Kerekes, T.; Sera, D.; Hameiri, Z. Solar cell cracks and finger failure detection using statistical parameters of electroluminescence images and machine learning. *Appl. Sci.* **2020**, *10*, 8834. [CrossRef]

28. Fernández, A.; Usamentiaga, R.; de Arquer, P.; Fernández, M.Á.; Fernández, D.; Carús, J.L.; Fernández, M. Robust detection, classification and localization of defects in large photovoltaic plants based on unmanned aerial vehicles and infrared thermography. *Appl. Sci.* **2020**, *10*, 5948. [CrossRef]
29. Kim, B.; Serfa Juan, R.O.; Lee, D.-E.; Chen, Z. Importance of image enhancement and CDF for fault assessment of photovoltaic module using IR thermal image. *Appl. Sci.* **2021**, *11*, 8388. [CrossRef]
30. Ballestín-Fuertes, J.; Muñoz-Cruzado-Alba, J.; Sanz-Osorio, J.F.; Hernández-Callejo, L.; Alonso-Gómez, V.; Morales-Aragones, J.I.; Gallardo-Saavedra, S.; Martínez-Sacristan, O.; Moretón-Fernández, Á. Novel utility-scale photovoltaic plant electroluminescence maintenance technique by means of bidirectional power inverter controller. *Appl. Sci.* **2020**, *10*, 3084. [CrossRef]
31. Henry, C.; Poudel, S.; Lee, S.-W.; Jeong, H. Automatic detection system of deteriorated PV modules using drone with thermal camera. *Appl. Sci.* **2020**, *10*, 3802. [CrossRef]
32. Hwang, M.-H.; Kim, Y.-G.; Lee, H.-S.; Kim, Y.-D.; Cha, H.-R. A study on the improvement of efficiency by detection solar module faults in deteriorated photovoltaic power plants. *Appl. Sci.* **2021**, *11*, 727. [CrossRef]
33. Liao, K.-C.; Lu, J.-H. Using UAV to detect solar module fault conditions of a solar power farm with IR and visual image analysis. *Appl. Sci.* **2021**, *11*, 1835. [CrossRef]
34. Hammami, M.; Torretti, S.; Grimaccia, F.; Grandi, G. Thermal and performance analysis of a photovoltaic module with an integrated energy storage system. *Appl. Sci.* **2017**, *7*, 1107. [CrossRef]
35. Kesavan, A.; Khanum, K.; Subbiahraj, S.; Ramamurthy, P. Evaluation of Polymer Solar Cell Efficiency To Understand the Burn-in Loss. *J. Phys. Chem. C* **2019**, *123*, 22699–22705. [CrossRef]
36. Hishikawa, Y.; Yamagoe, K.; Onuma, T. Non-contact measurement of electric potential of photovoltaic cells in a module and novel characterization technologies. *Jpn. J. Appl. Phys.* **2015**, *54*, 08KG05. [CrossRef]
37. Yasuda, S.; Okamoto, C.; Hishikawa, Y.; Negami, T.; Kawano, Y.; Minemoto, T. Hot-spot heat analysis on single crystalline Si based solar cell modules under partial shadi$^{\text{ng}}$, 21st "Next Generation Solar Power Generation System" Symposium. In Proceedings of the 4th Japan Photovoltaic Society Academic Conference, Kyoto, Japan, 29 June 2023.
38. Breitenstein, O.; Bauer, J.; Bothe, K.; Kwapil, W.; Lausch, D.; Rau, U.; Schmidt, J.; Schneemann, M.; Schubert, M.C.; Wagner, J.-M.; et al. Understanding junction breakdown in multicrystalline solar cells. *J. Appl. Phys.* **2011**, *109*, 71101. [CrossRef]
39. Wendlandt, S.; Giese, A.; Drobisch, A.; Tornow, D.; Hanusch, M.; Berghold, J.; Krauter, S.; Grunow, P. The temperature as the real hot spot risk factor at PV-modules. In Proceedings of the 27th European Photovoltaic Solar Energy Conference, Frankfurt, Germany, 24–28 September 2012.
40. Vieira, R.G.; De Araújo, F.M.; Dhimish, M.; Guerra, M.I. A Comprehensive Review on Bypass Diode Application on Photovoltaic Modules. *Energies* **2019**, *13*, 2472. [CrossRef]
41. Philipp, D.; Manuel, H.; Fokuhl, E.; Muelhoefer, G. Hot-spot endurance test—Modifications for bifacial photovoltaic modules. In Proceedings of the 35th European PV Solar Energy Conference and Exhibition, Brussels, Belgium, 24–28 September 2018; pp. 1029–1033.
42. Klasen, N.; Weisser, D.; Rößler, T.; Neuhaus, D.H.; Kraft, A. Performance of shingled solar modules under partial shading. *Prog. Photovolt. Res. Appl.* **2022**, *30*, 325–338. [CrossRef]
43. Bogachuk, D.; Saddedine, K.; Martineau, D.; Narbey, S.; Verma, A.; Gebhardt, P.; Herterich, J.P.; Glissmann, N.; Zouhair, S.; Markert, J.; et al. Perovskite Photovoltaic Devices with Carbon-Based Electrodes Withstanding Reverse-Bias Voltages up to –9 V and Surpassing IEC 61215:2016 International Standard. *Solar RRL* **2022**, *6*, 2100527. [CrossRef]
44. SunPower Performance Panel Technology for Large-Scale Installations, Maxeon Solar Technologies. Available online: https://sunpower.maxeon.com/int/sites/default/files/2022-03/COLLAT-100_Performance_Power_White_Paper_P6_Launch_FEB22_V15_FINAL.pdf (accessed on 3 September 2023).
45. International Electrotechnical Commission (IEC), IEC 61215-2:2016: Terrestrial Photovoltaic (PV) Moules-Design Qualification and Type Appoval-Part 2: Test Procedures. Available online: https://webstore.iec.ch/publication/61350 (accessed on 3 September 2023).
46. International Electrotechnical Commission (IEC), IEC 61730-2:2023 Photovoltaic (PV) Module Safety Qualification-Part 2: Requirements for Testing. Available online: https://webstore.iec.ch/publication/63895 (accessed on 3 September 2023).